## Iron binding to human heavy-chain ferritin

(Article begins on next page)

06 October 2024

# ARTICLE IN PRESS – Acta Cryst. D

### Iron binding to human heavy-chain ferritin

**Please check the following details for your article**
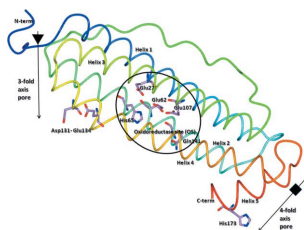


**Thumbnail image for contents page**

**Synopsis:** Time-lapse crystal structures of human H-chain ferritin loaded with iron show the distribution of the substrate metal ion within the catalytic site. Comparison of these data with previously determined X-ray structures of *R. catesbeiana* M ferritin points to a number of shared and unshared features of the active sites of the two proteins that contribute to the ongoing debate on the possible existence of a universal mechanism for iron oxidation in all ferritins.

**Abbreviated author list:** Pozzi, C.; Di Pisa, F.; Bernacchioni, C.; Ciambellotti, S.; Turano, P.; Mangani, S.

**Keywords:** ferritin; human heavy chain; iron; mechanism

# Iron binding to human heavy-chain ferritin

Cecilia Pozzi,[a] Flavio Di Pisa,[a] Caterina Bernacchioni,[b,c] Silvia Ciambellotti,[b,c] Paola Turano[b,c] and Stefano Mangani[a,c]*

[a]Dipartimento di Biotecnologie, Chimica e Farmacia, Università di Siena, Via Aldo Moro 2, 53100 Siena, Italy, [b]Dipartimento di Chimica, University of Florence, Via Della Lastruccia 3, Sesto Fiorentino, 50019 Firenze, Italy, and [c]CERM, University of Florence, Via Della Lastruccia 3, Sesto Fiorentino, 50019 Firenze, Italy. *Correspondence e-mail: stefano.mangani@unisi.it
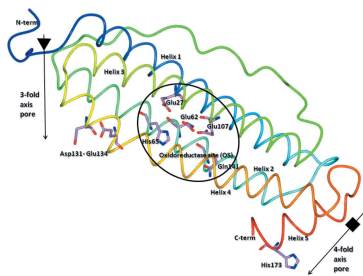
Maxi-ferritins are ubiquitous iron-storage proteins with a common cage architecture made up of 24 identical subunits of five $\alpha$-helices that drive iron biomineralization through catalytic iron(II) oxidation occurring at oxido-reductase sites (OS). Structures of iron-bound human H ferritin were solved at high resolution by freezing ferritin crystals at different time intervals after exposure to a ferrous salt. Multiple binding sites were identified that define the iron path from the entry ion channels to the oxidoreductase site. Similar data are available for another vertebrate ferritin: the M protein from *Rana catesbeiana*. A comparative analysis of the iron sites in the two proteins identifies new reaction intermediates and underlines clear differences in the pattern of ligands that define the additional iron sites that precede the oxidoreductase binding sites along this path. Stopped-flow kinetics assays revealed that human H ferritin has different levels of activity compared with its *R. catesbeiana* counterpart. The role of the different pattern of transient iron-binding sites in the OS is discussed with respect to the observed differences in activity across the species.

## 1. Introduction

Ferritins are ubiquitous chemical reactors that control the biosynthesis and dissolution of caged hydrated ferric minerals (EC 1.16.3.1). They also function as antioxidants by retrieving iron ions released from degraded iron proteins, preventing the occurrence of Fenton-like chemistry (Theil *et al.*, 2013).

The 24-subunit ferritins, called maxi-ferritins, self-assemble to form a nanocage with an outer diameter of approximately 120 Å, while the diameter of the internal cavity is around 80 Å (Liu & Theil, 2005). The ferritin nanocage is characterized by having 432 (*O*; octahedral) point symmetry with three fourfold, four threefold and six twofold axes (Crichton & Declercq, 2010). Thousands of Fe atoms can be stored in the inner cavity as an iron mineral obtained by catalytic oxidation of iron(II) by dioxygen or hydrogen peroxide in the protein oxidoreductase sites (OS; Fig. 1), where the substrates are coupled to obtain iron(III) mineral precursors (Theil *et al.*, 2013; Theil, 2011). In vertebrates, ferritin usually functions as a heteropolymer composed of two distinct subunits, the H (heavy, about 21 kDa) chain and the L (light, about 19 kDa) chain, that co-assemble in H:L ratios that are tissue-specific (Arosio *et al.*, 2009). Ferritin rich in L chain, which lacks oxidoreductase activity, is found in tissues involved in long-term storage of iron such as the liver or spleen, while H-chain-rich ferritin, with oxidoreductase activity, is found in tissues with more active iron metabolism such as muscle.
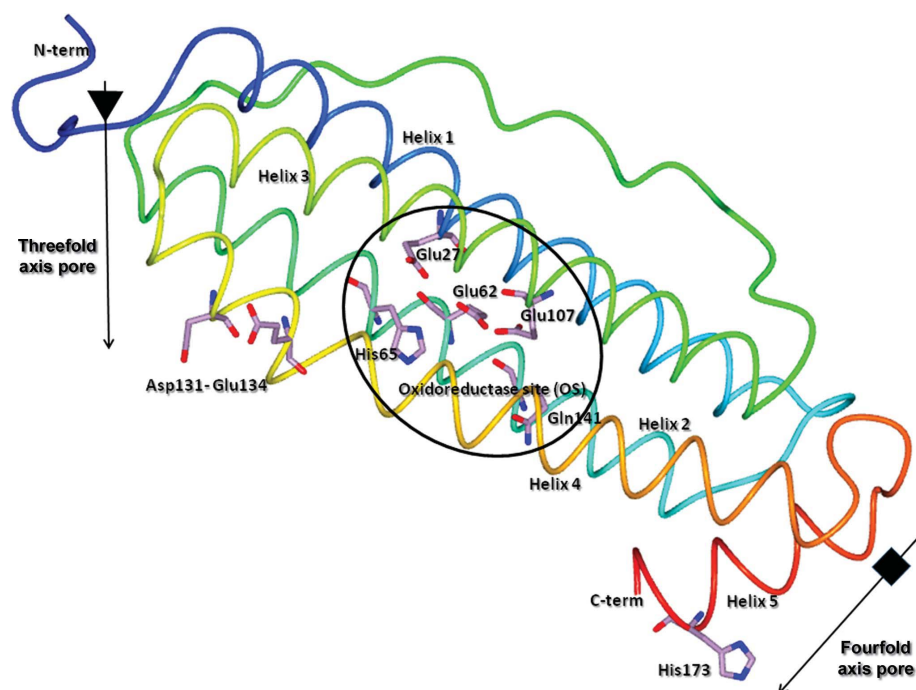
Iron-binding sites in maxi-ferritins have been identified by conventional X-ray crystallography only for those from the extremophilic archaeon *Pyrococcus furiosus* (Tatur *et al.*,

Files: d/dw5141/dw5141.3d d/dw5141/dw5141.sgml  **DW5141**  FA  IU-1514/12(30)7  1514/12(30)7  ()

**DW5141**  **PROOFS**  D:FA:2015:71:8:0:0–0

2007), the prokaryote *Escherichia coli* (Stillman *et al.*, 2001) and the eukaryote pennate diatom *Pseudo-nitzschia* (Marchetti *et al.*, 2009). The identification of iron-binding sites in other ferritins has been more difficult owing to the quite rapid turnover, which also occurs in the crystal and prevents the use of soaking–freezing experiments. Recently, a different approach has successfully revealed iron binding to *Rana catesbeiana* M ferritin (RcMf; Bertini *et al.*, 2012; Pozzi *et al.*, 2015). These studies have identified the existence of several iron-binding sites defining a possible pathway for iron(II) ions from the entry channels to the OS and have highlighted the role of several residues along this path.

There is an intense ongoing debate in the literature about the mechanism(s) by which the different ferritins operate. Recently, a so-called unifying mechanism for all ferritins has been proposed (Honarmand Ebrahimi *et al.*, 2012, 2015), but other views are also supported by the experimental evidence (Bou-Abdallah *et al.*, 2014; Bradley *et al.*, 2014; Pozzi *et al.*, 2015).

The wide ferritin panorama still lacks the identification of the iron-binding sites in a mammalian ferritin. To fill this gap, we report here the results of the crystallographic determination of iron adducts of human H ferritin (HuHf) obtained by applying the same experimental method as used in a previous study of RcMf (Pozzi *et al.*, 2015). Time-lapse anomalous data have allowed us to follow the progressive population of a series of iron-binding sites in a recombinant form of HuHf.

HuHf and RcMf share about 64% identity; the residues identified as active-site ligands in RcMf (*i.e.* Glu103, Glu58, His61 and Glu23) are all conserved in HuHf (the HuHf sequence numbering is shifted by +4 with respect to RcMf, as shown in Supplementary Fig. S1), but there are meaningful differences in the amino-acid composition of the OS residues proposed to be additional transient iron-binding sites in RcMf. The comparative analysis of the X-ray crystal structures and kinetic data for HuHf and RcMf presented here shows changes in the number and positions of these additional iron sites and in reaction rates. The implications for the proposed ferritin mechanism(s) are discussed.

## 2. Materials and methods

### 2.1. Protein expression and purification

RcMf was expressed as described previously (Pozzi *et al.*, 2015). The gene-coding sequence for HuHf was custom-synthesized (GenScript, USA) and subcloned into pET-9a expression vector using NdeI and BamHI restriction sites.

The expression plasmid was introduced by thermal shock into *E. coli* strain BL21 (DE3) (Invitrogen). Transformants were selected on LB agar supplemented with 50 mg l$^{-1}$ kanamycin. The bacterial culture was grown at 37°C on LB medium supplemented with 50 mg l$^{-1}$ kanamycin. Protein overexpression was induced with 0.2 m$M$ isopropyl $\beta$-D-1-thiogalactopyranoside (IPTG) when the cell density reached an $A_{600}$ of 0.6 with incubation at 30°C. The cells were harvested by centrifugation after 16 h of induction and were resuspended in buffer $A$ [20 m$M$ Tris pH 7.7, 1 m$M$ ethylenediaminetetraacetic acid (EDTA), 0.15 $M$ NaCl, 0.1 m$M$ phenylmethanesulfonyl fluoride hydrochloride (PMSF)]. The intracellular contents were liberated by sonication and the resulting suspension was centrifuged at 18 500$g$ for 45 min at 6°C to remove the insoluble fraction. The supernatant of the resulting crude extract was incubated at 60°C for 10 min and the heat-stable fraction was further purified by ammonium sulfate precipitation (50–60% saturated fractions), anion-exchange chromatography and size-exclusion chromatography as described previously for RcMf (Pozzi *et al.*, 2015).

### 2.2. Crystallization

Purified HuHf in 20 m$M$ Tris pH 7.7, 0.15 $M$ NaCl was



**Figure 1**
The HuHf subunit represented as a ribbon rainbow-coloured from the N-terminus (blue) to the C-terminus (red). The five $\alpha$-helices are sequentially numbered starting from the N-terminus. The oxidoreductase site (OS) and the threefold and fourfold pore locations are shown by arrows pointing into the interior of the ferritin cage together with the amino-acid residues involved in iron binding.

## Table 1
Data collection and processing.

Values in parentheses are for the outer shell.

| HuHf + iron(II) | 1 min | 5 min | 15 min | 30 min |
|---|---|---|---|---|
| PDB code | 4y08 | 4zjk | 4oyn | 4ykh |
| Diffraction source | I04-1, DLS | I04-1, DLS | I04-1, DLS | I04-1, DLS |
| Wavelength (Å) | 0.92 | 0.92 | 0.92 | 0.92 |
| Temperature (K) | 100 | 100 | 100 | 100 |
| Detector | Pilatus 2M | Pilatus 2M | Pilatus 2M | Pilatus 2M |
| Crystal-to-detector distance (mm) | 165 | 170 | 180 | 160 |
| Rotation range per image (°) | 0.20 | 0.20 | 0.20 | 0.20 |
| Total rotation range (°) | 100 | 100 | 100 | 100 |
| Exposure time per image (s) | 0.3 | 0.5 | 0.5 | 0.5 |
| Space group, $Z$ | $F432$, 4 | $F432$, 4 | $F432$, 4 | $F432$, 4 |
| No. of subunits in asymmetric unit | 1 | 1 | 1 | 1 |
| $a$, $b$, $c$ (Å) | 184.14 | 183.80 | 183.91 | 184.05 |
| Mosaicity (°) | 0.24 | 1.07 | 0.29 | 0.41 |
| Resolution range (Å) | 29.11–1.34 (1.41–1.34) | 31.07–1.56 (1.64–1.56) | 32.51–1.43 (1.51–1.43) | 29.10–1.52 (1.60–1.52) |
| Total No. of reflections | 1205847 (172066) | 437700 (36197) | 990962 (142832) | 809546 (102979) |
| No. of unique reflections | 60022 (8623) | 38257 (5431) | 49578 (7123) | 41531 (5956) |
| Completeness (%) | 99.7 (100.0) | 99.8 (99.1) | 100.0 (100.0) | 100.0 (100.0) |
| Anomalous completeness (%) | 99.8 (100.0) | 99.0 (95.7) | 100.0 (100.0) | 100.0 (100.0) |
| Multiplicity | 20.1 (20.0) | 11.4 (6.7) | 20.0 (20.1) | 19.5 (17.3) |
| Anomalous multiplicity | 10.6 (10.3) | 5.9 (3.4) | 10.5 (10.3) | 10.3 (8.8) |
| $\langle I/\sigma(I)\rangle$ | 28.2 (8.0) | 25.0 (3.6) | 27.9 (7.1) | 25.8 (7.0) |
| $R_{meas}$ | 0.072 (0.414) | 0.062 (0.510) | 0.072 (0.438) | 0.082 (0.434) |
| Overall $B$ factor from Wilson plot (Å$^2$) | 8.5 | 11.0 | 9.7 | 10.3 |

## Table 2
Structure solution and refinement.

Values in parentheses are for the outer shell.

| HuHf + iron(II) | 1 min | 5 min | 15 min | 30 min |
|---|---|---|---|---|
| PDB code | 4y08 | 4zjk | 4oyn | 4ykh |
| Resolution range (Å) | 27.76–1.34 (1.38–1.34) | 31.07–1.56 (1.60–1.56) | 31.09–1.43 (1.47–1.43) | 28.07–1.52 (1.56–1.52) |
| Completeness (%) | 99.7 (100.0) | 99.7 (98.3) | 100.0 (100.0) | 99.9 (100.0) |
| $\sigma$ Cutoff | 2.0 | 2.0 | 2.0 | 2.0 |
| No. of reflections, working set | 56945 (4127) | 36303 (2592) | 47040 (3384) | 39434 (2874) |
| No. of reflections, test set | 3037 (230) | 1918 (124) | 2508 (190) | 2086 (139) |
| Final $R_{cryst}$ | 0.163 (0.175) | 0.168 (0.202) | 0.167 (0.183) | 0.165 (0.171) |
| Final $R_{free}$ | 0.173 (0.190) | 0.192 (0.237) | 0.179 (0.214) | 0.187 (0.180) |
| Cruickshank DPI | 0.043 | 0.068 | 0.053 | 0.062 |
| No. of non-H atoms | | | | |
|   Protein | 1409 | 1413 | 1413 | 1410 |
|   Ion | 19 | 24 | 23 | 23 |
|   Ligand | 4 | — | 19 | 11 |
|   Water | 328 | 329 | 320 | 323 |
|   Total | 1760 | 1766 | 1775 | 1676 |
| R.m.s. deviations | | | | |
|   Bonds (Å) | 0.006 | 0.007 | 0.005 | 0.006 |
|   Angles (°) | 1.037 | 1.000 | 0.981 | 1.007 |
| Average $B$ factors (Å$^2$) | | | | |
|   Protein | 10.2 | 13.7 | 11.7 | 12.9 |
|   Ion | 13.9 | 20.3 | 16.1 | 16.4 |
|   Ligand | 9.2 | 0.0 | 22.5 | 9.5 |
|   Water | 23.6 | 29.4 | 26.2 | 27.8 |
| Estimate error on coordinates based on $R$ value (Å) | 0.043 | 0.068 | 0.053 | 0.062 |
| Ramachandran plot | | | | |
|   Most favoured (%) | 98.8 | 98.8 | 98.8 | 98.8 |
|   Allowed (%) | 1.2 | 1.2 | 1.2 | 1.2 |

concentrated to 13.4 mg ml$^{-1}$. Crystals of native HuHf were grown using the hanging-drop vapour-diffusion technique at 297 K. Drops were prepared by mixing equal volumes (2 µl) of HuHf and a precipitant solution composed of 2.0 $M$ MgCl$_2$,

0.1 $M$ bicine pH 9.0 to give a final pH value of about 8.0. Octahedrally shaped crystals of 50–100 µm in size grew in 3–6 d. The crystallization of HuHf was also performed under strict anaerobic conditions using the same procedure as previously reported for RcMf (Pozzi et al., 2015). These crystals were used as a control for the oxidation state and coordination environment of iron in the aerobic crystals.

A time-controlled iron-loading study was performed by allowing solid-to-solid iron(II) ion diffusion from grains of [(NH$_4$)$_2$Fe(SO$_4$)$_2$]·6H$_2$O (Mohr's salt) to HuHf crystals of approximately the same size ($\sim$100 µm) for monitored exposure times of 1, 5, 15 and 30 mins, and for up to 8 min for the anaerobic crystals, followed by flash-cooling in liquid nitrogen, as reported previously for RcMf (Pozzi et al., 2015).

### 2.3. Data collection, structure solution and refinement

Complete data sets were collected on beamline I04-1 at Diamond Light Source (DLS) using a Pilatus 2M detector at 100 K. Data were integrated using MOSFLM v.7.0.4 (Leslie, 2006) and scaled with SCALA (Evans, 2006, 2011) from the CCP4 suite (Winn et al., 2011). The HuHf crystals belonged to the cubic space group $F432$, with unit-cell parameter $a \simeq 185$ Å, varying slightly among the different crystals. Data-collection and processing statistics are reported in Table 1. Anomalous difference maps were computed from the single-wavelength data exploiting the iron anomalous signal, which was still present at 0.920 Å (13.477 keV; $f' \simeq -0.298$ e$^-$, $f'' \simeq 1.35$ e$^-$) and nevertheless provides very clear anomalous maps owing to the high quality and the redundancy of the data collected. All of the iron-binding sites found in these maps have subsequently been fully confirmed by lower resolution

data sets collected in a two-wavelength measurement mode (Fe $K$ edge and remote) at Elettra, Trieste, Italy from crystals treated with iron under exactly the same conditions.

Phasing was performed by molecular replacement using *MOLREP* (Vagin & Teplyakov, 2010) from the *CCP*4 suite. A subunit of human H ferritin (PDB entry 3ajo; Masuda *et al.*, 2010) was used as a search model, excluding nonprotein atoms and water molecules. The positions of the iron ions were determined from anomalous difference Fourier maps computed using *FFT* from the *CCP*4 suite. The anomalous signals corresponding to iron ions were between 6$\sigma$ and 40$\sigma$ in the anomalous difference maps.



(a)

(b)
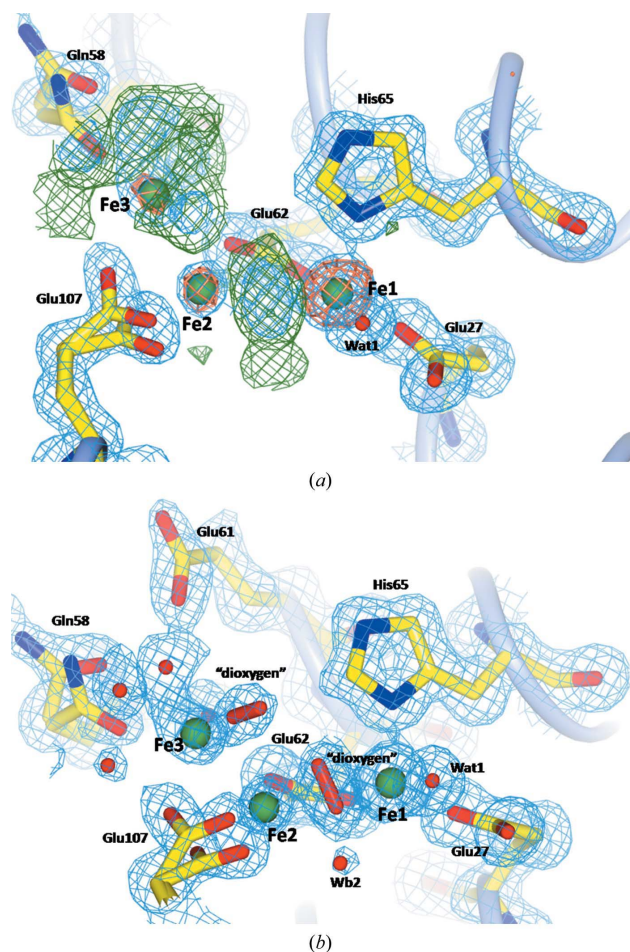
**Figure 2**
(a) Electron density in the HuHf oxidoreductase site after 1 min of free diffusion of iron into the crystals. The $2F_o - F_c$ map is represented as a light blue mesh (1.5$\sigma$), while the residual $F_o - F_c$ difference map contoured at 3.0$\sigma$ is represented as a green mesh. The copper mesh represents the anomalous difference map contoured at 4.0$\sigma$. The protein backbone is represented as a light blue cartoon and residues involved in iron coordination are highlighted as yellow sticks. The disorder present in some side chains is visualized as double conformations. Iron ions are represented as green spheres. (b) Our interpretation of the electron-density maps shown in (a). Two 'dioxygen-like' molecules are represented as sticks. The $2F_o - F_c$ map is contoured at 1.5$\sigma$ (light blue mesh). The $F_o - F_c$ Fourier difference map is featureless at 3.0$\sigma$.

The structures were refined with *REFMAC* v.5.8 (Murshudov *et al.*, 2011). The refinement protocol involved sequential iterative manual rebuilding of the model and maximum-likelihood refinement. Manual rebuilding and modelling of the missing atoms into the electron density was performed with the molecular-graphics software *Coot* (Emsley *et al.*, 2010). Partial occupancies for the iron or magnesium ions, for other ligands and for several amino-acid residues were adjusted in order to obtain atomic displacement parameters that were close to those of neighbouring protein atoms in fully occupied sites. The occupancies of the water molecules or other ligands bound to metal ions were kept the same as those of the parent metal ion. *ARP/wARP* was used for the addition of water molecules (Langer *et al.*, 2008). The final models were inspected manually and checked with *Coot* and *PROCHECK* (Laskowski *et al.*, 1993). The final refinement statistics are reported in Table 2. All figures were generated using *CCP*4*mg* (McNicholas *et al.*, 2011).

### 2.4. Stopped-flow kinetics

The addition of 1–4 iron(II) ions per subunit (Bernacchioni *et al.*, 2014, 2015; Theil *et al.*, 2014) to HuHf and RcMf was monitored by the change in $A_{650\,nm}$ (diferric peroxo; DFP) or $A_{350\,nm}$ [diferric oxo/hydroxo species; DFO(H)] after rapid mixing (less than 10 ms) of equal volumes of 100 μ$M$ protein subunits (4.16 μ$M$ protein cages) in 200 m$M$ 3-($N$-morpholino)propanesulfonic acid (MOPS), 200 m$M$ NaCl pH 7.0 with freshly prepared solutions of 100, 200, 300 or 400 μ$M$ ferrous sulfate in 1 m$M$ HCl in a UV–visible stopped-flow spectrophotometer (SX.18MV stopped-flow reaction analyzer; Applied Photophysics, Leatherhead, England). Routinely, 4000 data points were collected during the first 5 s. The initial formation rates of DFP and DFO(H) species were determined from linear fitting of the initial phases (0.01–0.03 s) of the change in absorbance at 650 and 350 nm, respectively. The decay rate of the DFP species was fitted with a monoexponential function of the decrease in intensity at 650 nm (Tosha *et al.*, 2012).

### 2.5. Transmission electron microscopy (TEM)

Recombinant ferritin protein cages (3 μ$M$) were mineralized with ferrous sulfate [80 iron(II) ions per subunit] in 100 m$M$ MOPS, 100 m$M$ NaCl pH 7.0. Two different procedures were followed: (i) a total of 80 iron(II) ions per subunit were added in a single step or (ii) three sequential additions were performed [20 iron(II) ions per subunit, 20 iron(II) ions per subunit and 40 iron(II) ions per subunit]. After each addition the solutions were incubated for 2 h at room temperature and then overnight at 4°C to complete the iron-mineralization reaction. For TEM tests, solutions of mineralized HuHf and RcMf cages were dropped onto and dried on a Cu grid covered by a holey carbon film. Bright-field TEM images were collected using a Philips CM12 microscope operating at 80 kV (Bernacchioni *et al.*, 2014).

## 2.6. PDB codes

The final coordinates and structure factors for HuHf loaded with iron ions for 1, 5, 15 and 30 min have been deposited in the PDB under accession codes 4p03, 4zjk, 4oyn and 4ykh, respectively.

## 3. Results

### 3.1. Overall structure of human H ferritin

A series of HuHf structures were obtained at high resolution by following an established protocol that allows us to use time-lapse crystallography to appreciate the succession of iron-binding events (Pozzi *et al.*, 2015). Crystals of iron-free HuHf were mixed with crystalline ferrous ammonium sulfate powder (Mohr's salt) and frozen after 1, 5, 15 and 30 min of free diffusion of iron(II) ions into the crystallization drop in the presence of the second reaction substrate, dioxygen (see §2).

The structure of iron-free HuHf (not described) was obtained as a reference structure and shows the same quaternary structure as all other maxi-ferritins, consisting of the assembly of 24 identical subunits to form a hollow cage. The asymmetric unit contains a single HuHf subunit which represents the spatial and time average of all subunits of the molecule in the crystal. The HuHf subunit reported in Fig. 1 shows the characteristic four-helix bundle (helices 1–4) tertiary structure completed by a fifth helix (helix 5) (Theil *et al.*, 2013).

Each of the four structures determined in this work contains a variable number of metal ions [magnesium and/or iron(II)/iron(III)]; the chemical nature of the metal was discriminated according to the anomalous signal detected. The oxidation state of the iron ions was more elusive and was derived from comparison with the structure obtained under anaerobic conditions (see below). The refined structures are all nearly complete as according to the electron density for all structures the polypeptide chain has been built starting from residue 5 to residue 176. No significant changes in the fold of the HuHf subunit were observed upon exposure to the iron salt.

### 3.2. HuHf iron binding at the ferroxidase at different diffusion times

The structure obtained after free diffusion of iron(II) ions for about 1 min under aerobic conditions has been refined to 1.34 Å resolution. Fig. 2(*a*) shows a view of the OS with the iron ions found from the anomalous difference map computed from data collected above the Fe *K* edge. The $2F_o - F_c$ and Fourier difference maps are superimposed on the anomalous map. The largest anomalous signal ($28\sigma$) identifies an iron ion bound at iron site 1 (Fe1) defined by Glu27 (monodentate ligand from helix 1), Glu62 (monodentate ligand from helix 2) and His65 (from helix 2). A water molecule (Wat1 in Fig. 2*a*) bound to Fe1 is clearly visible. A much weaker anomalous signal ($6.5\sigma$) corresponds to the Fe ion bound to the nearby site 2 (Fe2), where it is held by the Glu62 carboxylate, forming a bridge to Fe1, and by coordination bonds to Glu107 (as a bidentate ligand from helix 3). Fe1 and Fe2 refine to occupancies of about 0.7 and 0.2, respectively, and are located at a distance of 3.48 Å. These two sites are the same as the Fe1 and Fe2 sites found in RcMf. At variance with the RcMf structure obtained under the same experimental conditions (Pozzi *et al.*, 2015), no magnesium ions from the crystallization solution are found bound in the OS. In addition, a large maximum between Fe1 and Fe2 that cannot be accounted for by a bridging water/hydroxide molecule is present in the Fourier difference map (Fig. 2*a*). This maximum indicates that the completion of the coordination spheres of Fe1 and Fe2 might involve other ligands.

Fig. 2(*b*) shows a view of the ferroxidase site after completing the refinement that reports our best interpretation of the difference Fourier map. The elongated maximum of continuous electron density between Fe1 and Fe2 (Fig. 2*a*) suggests the presence of a diatomic molecule and persists even when two water molecules at partial occupancy (too close to be independent) were inserted. We were then tempted to model this density as a peroxide anion or a dioxygen molecule. Finally, our best model consists of a diatomic 'dioxygen' molecule bound to Fe1 and Fe2 in a $\mu$-$\eta_2$:$\eta_2$ configuration (bridging side-on) with the same occupancy as Fe2 (0.2) and of a bridging water/hydroxide at the same occupancy as Fe1 (0.7) (hidden by the 'dioxygen' in Fig. 2*b*). A second bridging water/hydroxide at low occupancy (0.3) can account for residual electron density between the iron ions (Wb2 in Fig. 2*b*). As can be seen from Fig. 2(*b*), this model accounts for the maxima of the $F_o - F_c$ map in this part of the cavity.

Inspection of the anomalous difference map (see Fig. 2*a*) reveals the presence of a third Fe ion (Fe3, $5.5\sigma$) bound to the nearby Gln58 residue found disordered over two positions (iron-bound and unbound). Fe3 is close to Fe2 (2.73 Å) and can be refined to an occupancy of 0.3. Here, the $F_o - F_c$ map shows several maxima that are difficult to interpret, revealing disorder in this site (Fig. 2*a*). In addition to the Gln58 side chain, one conformer of Glu107 is within coordination distance of Fe3 and the well ordered side chain of Glu62 lies at about 2.65 Å. Two water molecules and one 'dioxygen' molecule with the same occupancy as the metal ion can be refined as Fe3 ligands to attain hexacoordination. However, after refinement the residual $F_o - F_c$ map still presents very diffuse maxima of positive electron density in the surroundings of Fe3. A fourth iron ion (Fe4) is found bound with 0.3 occupancy to the nearby His57 residue that extends into the cage cavity at about halfway between the threefold pore (22 Å) and the fourfold pore (24 Å) (not shown in Figs. 2*a* and 2*b*).

The 1 min exposure experiment was repeated twice in order to verify the reproducibility of the quite puzzling results obtained, and the Fourier maps obtained displayed the same features.

However, although suggestive, our interpretation of the electron-density maps cannot be claimed as clear evidence for the trapping of the dioxygen substrate in the HuHf OS before reaction (see §4). On the other hand, the interpretation described above leads to the best minimum of the refinement

quality indicators and it can be framed as the superposition of different states occurring in HuHf subunits: in about 30% of them no iron is bound, in about 70% of them the OS Fe site 1 is occupied by iron and in about 20% the OS Fe site 2 (which is empty in 80% of the cases) also binds iron. In the 50% of the cases where only site 1 is occupied a water molecule completes the Fe1 coordination, while in the 20% of the cases where both sites 1 and 2 are occupied a dioxygen molecule might bind in $\mu$-$\eta_2$:$\eta_2$ coordination mode to both Fe1 and Fe2. It should be noted that the shape of the electron density interpreted as dioxygen is the same or even better when compared with the electron density of 'dioxygen' molecules bound to enzymes such as naphthalene dioxygenase (PDB entry 1o7m; Karlsson *et al.*, 2003) or cytochrome P450cam (PDB entries 1dz8 and 2a1m; Nagano & Poulos, 2005; Schlichting *et al.*, 2000).

Fe site 3 might represent the 30% of the subunits in which the Fe1 and Fe2 sites are not yet occupied by iron. This is supported by the double conformation of Glu107 that appears to take Fe3 from Gln58 and drive it to the Fe2 site (Figs. 2a and 2b).

In any case, this crystal structure confirms that Gln58 is involved in iron shuttling into the OS Fe1 and Fe2 iron-binding sites in a dynamic process, as shown by the structural disorder present in this portion of the cavity and as already suggested by our previous experiments on RcMf, where His54 takes the role of Gln58, and on the RcMf His54/Gln54 variant (Pozzi *et al.*, 2015). In other words, the different HuHf subunits of our crystal are trapped in different states related to their interaction, with iron(II) ions providing a superposition of images that show the conformational variability of the residues involved in iron processing.

The anomalous difference map of HuHf measured after 5 min of free diffusion of iron(II) reveals a clearer picture of the ferroxidase site, although some disorder is still present. The map confirms the sites already observed in the previous structure, but the occupancies are now much higher (Fig. 3a). Fe1 is fully occupied, while Fe2, Fe3 and Fe4 reach 50% occupancy. The coordination spheres of all iron ions are also better defined, as shown in Fig. 3(b). Fe1 displays a 5 + 1 coordination sphere with five ligands (Glu27, Glu62, His65, Wb1 and Wat1) arranged in a square-pyramidal geometry (with His65 at the apex) and a further water molecule (Wb2) at a longer distance that forms an asymmetric second bridge to Fe2. The Fe2 coordination can be described as trigonal bipyramidal, with Glu62, Glu107 (considering the bidentate Glu107 as one ligand) and Wb1 in the basal plane and Wb2 and Wat2 at the apices. The same Fe1 and Fe2 ligands have previously been observed to bind iron ions in RcMf in the same fashion (Pozzi *et al.*, 2015), with the exception of Wb2, which has never been observed in other ferritins. In the 5 min structure, the 'biatomic' molecule bridging Fe1 and Fe2 in the 1 min structure has been replaced by the Wb1 species (water/hydroxide). Both Wb1 and Wb2 have gained full occupancy: Wb1 is hydrogen-bonded to the side chain of Gln141, while Wb2 is at a contact distance to Val110. The Fe1–Fe2 distance is 3.49 Å. A hydrogen-bonding network links Gln141, the bidentate Fe2 ligand Glu107 and Tyr34. Tyr34 and Gln141

together with the other residues involved in Fe1 and Fe2 binding are highly conserved in H/M-type ferritins (Ebrahimi *et al.*, 2012; see Supplementary Fig. S1).

The position of Fe3 has now changed to give a different and better defined coordination environment (see Figs. 3a and 3b). Fe3 is in a new position located 6.61 Å away from Fe2, being bound at coordination distances to Gln58 (now ordered) and Glu61, the only protein ligands in this site, and surrounded by four water molecules that complete a quite regular octahedral coordination. The involvement of Glu61 in HuHf in the attraction of iron towards the OS is similar to that observed for the corresponding Glu57 in RcMf.



(a)



(b)
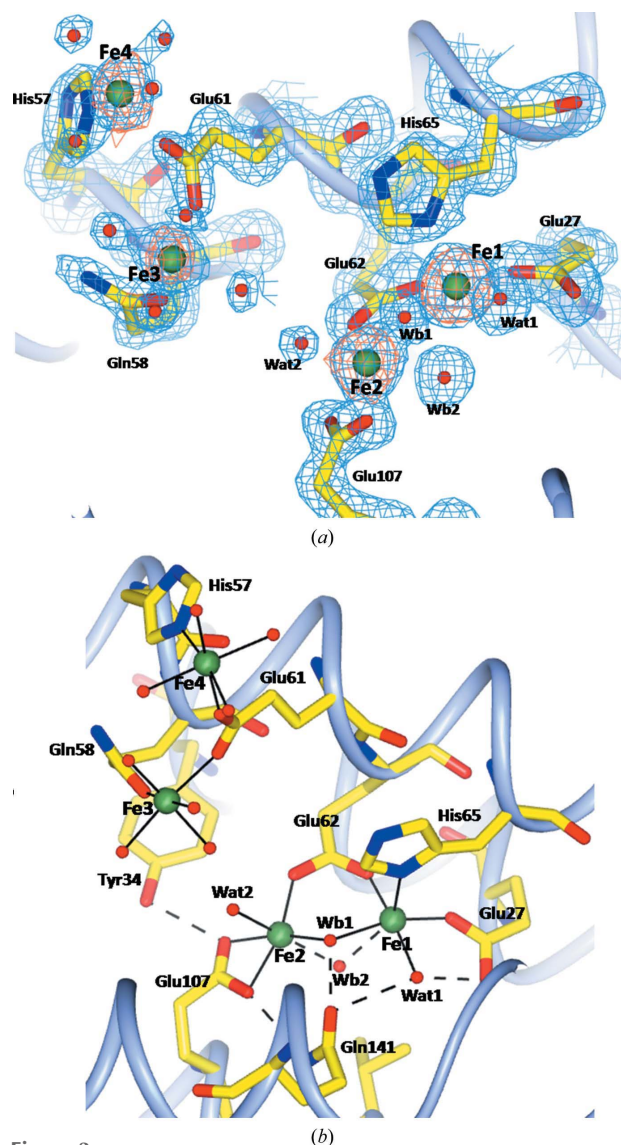
**Figure 3**
(a) Electron density in the HuHf oxidoreductase site after 5 min of exposure to Mohr's salt. The Fourier maps and anomalous difference map contours and colours are the same as in Fig. 1. (b) Schematic view of the OS of HuHf. Coordination bonds are shown as black continuous lines; hydrogen bonds are represented by dotted lines. The colour codes are the same as used in Fig. 1.

Fe4 is 5.08 Å from Fe3 and is bound to Glu61, which bridges it to Fe3. His57 and four water molecules are the remaining ligands that also define an octahedral coordination geometry for this site.

Increasing the iron(II) diffusion time (to 15 and 30 min) leads to no further changes in the iron-binding sites in the OS and surroundings. All iron ions, Fe1 to Fe4, maintain the same coordination environments, indicating that after about 5 min a dynamical equilibrium has been reached in the protein crystals.

In summary, the occupancy of Fe1 to Fe4 does not vary after 5 min of exposure to Mohr's salt. The Fe1 site is about 70% occupied after 1 min and is fully occupied from 5 min onwards. On the contrary, the Fe2 occupancy ranges from about 20% in the structures determined after a short diffusion time to a maximum of about 50%. The same occurs for the Fe3 and Fe4 occupancies, which achieve a maximum of 50%. At variance with the observations made for iron-bound RcMf (Pozzi *et al.*, 2015), both the Wb1 and the Wb2 molecules make asymmetric bridges between Fe1 and Fe2, with both being closer to Fe2. There are not evident structural reasons to justify this behaviour. A possible explanation could be that in all HuHf structures (except for the 1 min structure) we are observing a mixed-valence Fe1[iron(II)]–Fe2[iron(III)] cluster instead of the Fe1[iron(II)]–Fe2[iron(II)] cluster suggested by the RcMf crystal structures (Pozzi *et al.*, 2015). The increased positive charge of the site may also explain the presence of Wb2 (possibly a hydroxide anion), which is never observed in RcMf.

The high-resolution structure (1.2 Å) of iron-bound HuHf, which was obtained after 8 min of exposure to Mohr's salt from crystals obtained under strict anaerobic conditions (data not shown), was used as a check for the oxidation state of iron in the aerobically grown crystals. This structure shows iron ions bound only to Fe sites 1 and 2, with occupancies of about 80% for Fe1 and of about 30% for Fe2. The Fe1–Fe2 distance is 3.52 Å and, more importantly, only one water/hydroxide molecule is found symmetrically bridging the two irons, at variance with the aerobic crystals. Fe1 and Fe2 adopt the same coordination geometry as observed for RcMf (Pozzi *et al.*, 2015).

### 3.3. Threefold-symmetry channels

The threefold-symmetry channels have been identified as the main entrance of iron ions into the protein shell (Haldar *et al.*, 2011; Theil, 2011). The structure of iron-free HuHf shows two magnesium hexaaqua ions, arising from the crystallization buffer, inside this negatively charged protein pore defined by the side chains of the three symmetry-related Asp131, Glu134 and Thr135 residues. A third magnesium hexaaqua ion is found just beyond the channel on the internal protein surface. The positions of these magnesium ions in the threefold pore are remarkably consistent with those previously reported for HuHf (Masuda *et al.*, 2010). The same three magnesium hexaaqua ions have also consistently been observed in the structure of HuHf exposed to iron(II) ions for 1 and 5 min. On

the contrary, in the structures determined after 15 and 30 min of iron loading two iron(II) hexaaqua ions have replaced the magnesium aqua ions inside the channel, as indicated by the strong anomalous peaks that are present in these sites (Figs. 4*a* and 4*b*). The occupancy for both iron(II) aqua ions inside the channel refines to 0.6. The observation of iron in the threefold channel has previously been reported after a longer exposure time to iron (60 min) for RcMf and its H54Q variant (Pozzi *et al.*, 2015).

### 3.4. Fourfold-symmetry channels

The fourfold pores of the ferritin cage are defined by four helices 5 (Fig. 1) from symmetry-related subunits which make a four-helix bundle around the fourfold axes. The part of the fourfold channel facing the external surface of the ferritin cage is highly hydrophobic, as in RcMf, being constituted by four symmetry-related Leu165 and Leu169 residues. Like RcMf, the internal portion of the channel has a hydrophilic character, being constituted by four symmetry-related His173 residues.



(a)



(b)
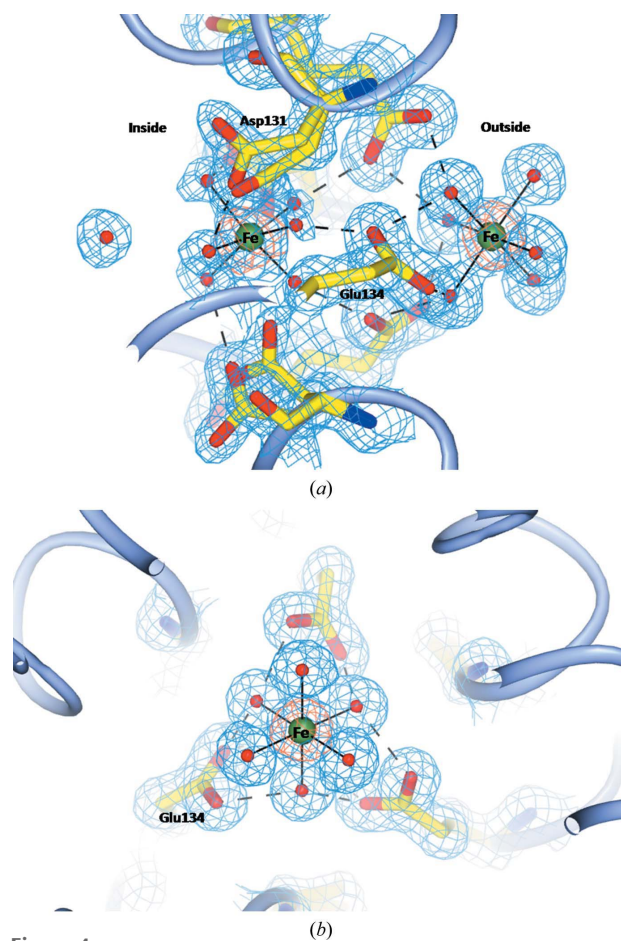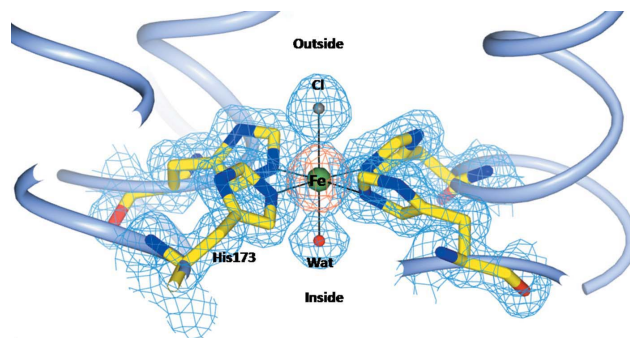
**Figure 4**
Views perpendicular (*a*) and parallel (*b*) to the threefold-axis pore of HuHf as appearing in the crystal structure obtained after 15 min of free diffusion of iron ions inside the crystal. The $2F_o - F_c$ and the anomalous difference maps are superimposed on the atomic model. The cutoffs and the colour codes are the same as used in the previous figures.

In the iron-free HuHf structure two chloride ions (identified by the anomalous signal) from the crystallization buffer are located above and below the plane of the four His173 residues.

The binding of iron ions in the fourfold channel develops with time. The anomalous difference map of the 1 min HuHf structure shows a very weak trace of the presence of iron ions bound to a tiny fraction (less than 10%) of the His173 residues. However, after 5 min the fourfold pore is fully occupied by an iron(II) ion bound to the four symmetry-related His173 residues defining the plane of a tetragonal bipyramid; at the apices are one chloride anion and one water molecule directed towards the external and the internal surface of the cage, respectively (Fig. 5). This kind of coordination environment for iron bound to the fourfold pore is identical to that previously observed in iron-loaded RcMf (Pozzi *et al.*, 2015), and is consistent with the presence of iron(II) ions in this pore. No iron transport into the inner cage occurs through these types of channels (Theil *et al.*, 2014).

### 3.5. Reactivity in solution

For both RcMf and HuHf, stopped-flow kinetic measurements reveal that the same intermediate species form during the reaction, although with different kinetics. With a stoichiometry of one iron(II) ion per subunit, the activity at the OS is essentially negligible for both proteins (Figs. 6*a* and 6*b*). With two iron(II) ions per subunit or more, we can clearly observe the formation of the DFP intermediate and its rapid decay through a monoexponential process as well as the formation of the ferric oxo species. The initial rate of formation in RcMf increases essentially linearly when going from two to four iron(II) ions per subunit (Fig. 6*b*); the increase in initial rate is less regular for HuHf. While for the latter protein the formation rate of DFP is slightly faster at a low iron(II) ratio, it levels off with four iron(II) ions per subunit. On the contrary, the exponential decay of DFP is always slower in the HuHf protein, and this difference increases on increasing the number of iron(II) per subunit (Figs. 6*a* and 6*b*). The initial rate of formation of DFO(H) species grows linearly with number of iron(II) per subunit but with different slopes for



**Figure 5**
View of the fourfold-axis pore of HuHf as appearing in the crystal structure obtained after 5 min and onwards. The $2F_o - F_c$ and the anomalous difference maps are superimposed on the atomic model. The cutoffs and the colour codes are the same as used in the previous figures.

the two proteins (Fig. 6*b*). In spite of the different rates of the catalytic reactions, the end product of the biomineralization reaction is an iron-oxo core of comparable size with the same iron:protein ratio: 4.74 $\pm$ 0.26 nm for HuHf *versus* 5.37 $\pm$ 0.29 nm for RcMf, as shown in Fig. 7.

## 4. Discussion

Observing iron-binding sites in most vertebrate maxi-ferritins is made difficult by the quite rapid reaction rates measured in solution (<25 ms for RcMf; Hwang *et al.*, 2000) that prevent the use of conventional soaking or co-crystallization approaches. We have thus developed a solid-to-solid free-diffusion technique that allows the trapping of iron ions in their diffusion pathways through ferritin by freezing the protein crystals at different times after exposure to iron (Pozzi *et al.*, 2015).

The sequence of iron-binding events monitored by our experiments reported here starts with the partial occupancy of oxidoreductase sites 1 and 2 by iron; the higher occupancy for Fe1 observed in the 1 min structure, which reaches full occupancy after 5 min, confirms all previous thermodynamic data (Bou-Abdallah, Arosio *et al.*, 2002; Bou-Abdallah *et al.*, 2003; Honarmand Ebrahimi *et al.*, 2012) and structural data (Pozzi *et al.*, 2015) about the higher affinity of this site for metal ions in vertebrate ferritins. This is easily explained by the three protein ligands present in Fe site 1 with respect to the two protein ligands present in Fe site 2 (Pozzi *et al.*, 2015; Treffry *et al.*, 1997). Selective population of a single site in the OS is also consistent with the kinetic data (Figs. 6*a* and 6*b*) which, at variance with previous Mössbauer data (Bou-Abdallah, Papaefthymiou *et al.*, 2002), show the absence of any ferroxidase activity when one iron(II) ion per subunit is added. Similarly, the observation of a high-affinity iron-binding site corresponding to the HuHf site 1 has previously also been reported in the structures of ferritin from other organisms, such as *Pseudo-nitzschia multiseries* (Marchetti *et al.*, 2009; Pfaffen *et al.*, 2013), *E. coli* (Stillman *et al.*, 2001) and *P. furiosus* (Tatur *et al.*, 2007).

The 1 min crystal structure evokes a fascinating hypothesis about a possible binding mode for the substrate dioxygen in the OS and suggests that this substrate binds the dinuclear oxidoreductase centre only when iron site 2 is occupied by iron(II) ions, possibly linked to the movement of iron from the provisional site 3 to site 2. A $\mu$-$\eta_2$:$\eta_2$ side-on coordination mode to a first-row transition-metal ion has been observed for dioxygen or peroxide only in a copper laccase (PDB entry 3zdw) and in model complexes of dinuclear copper centres (Mirica *et al.*, 2004, 2006). This binding mode of dioxygen might evolve in the peroxo-diferric intermediate structure suggested by vibrational and XAS spectroscopies (structures E or G in Fig. 3 of Hwang *et al.*, 2000).

The observation of a short Fe3–Fe2 distance in the 1 min structure (2.73 Å) that lengthens to 6.61 Å in the 5 min structure suggests that the former structure has trapped the iron(II) ion (Fe3 in Figs. 2*a* and 2*b*) approaching the empty Fe2 site, possibly dragging an already bound dioxygen molecule with it.

The similarity of the 5, 15 and 30 min HuHf structures indicates that after a short time lapse a dynamical equilibrium is reached in the iron diffusion inside the crystals and a steady-state-like situation is established. The incoming iron(II) ions are processed and stored as a ferric mineral inside the ferritin cage, as indicated by the rusty colour that is gained by the crystals with time.

Taken together, the time-lapse pictures from the present study delineate a pathway for the incoming iron(II) ions that starts with the electrostatic attraction and hydrogen-bonding interactions of the iron(II) hexaaqua ions with the Asp131 and Glu134 residues in the threefold pore and continues with Glu140, Glu61, His57 and Gln58 to reach the Fe1 and Fe2 sites.

The coordination of the Fe1 and Fe2 sites observed in HuHf shows relevant differences with respect to the same sites in RcMf determined under the same experimental conditions. While Fe1 and Fe2 in RcMf are linked by a double symmetric bridge (Glu58 and a water/hydroxide molecule), a triple asymmetric bridge is found between Fe1 and Fe2 in HuHf (Glu62 and two water/hydroxide molecules; see Fig. 3b). Furthermore, Fe1 in HuHf shows a 5 + 1 type of coordination sphere in contrast to RcMf, where Wb2 (Figs. 3a and 3b) is absent.
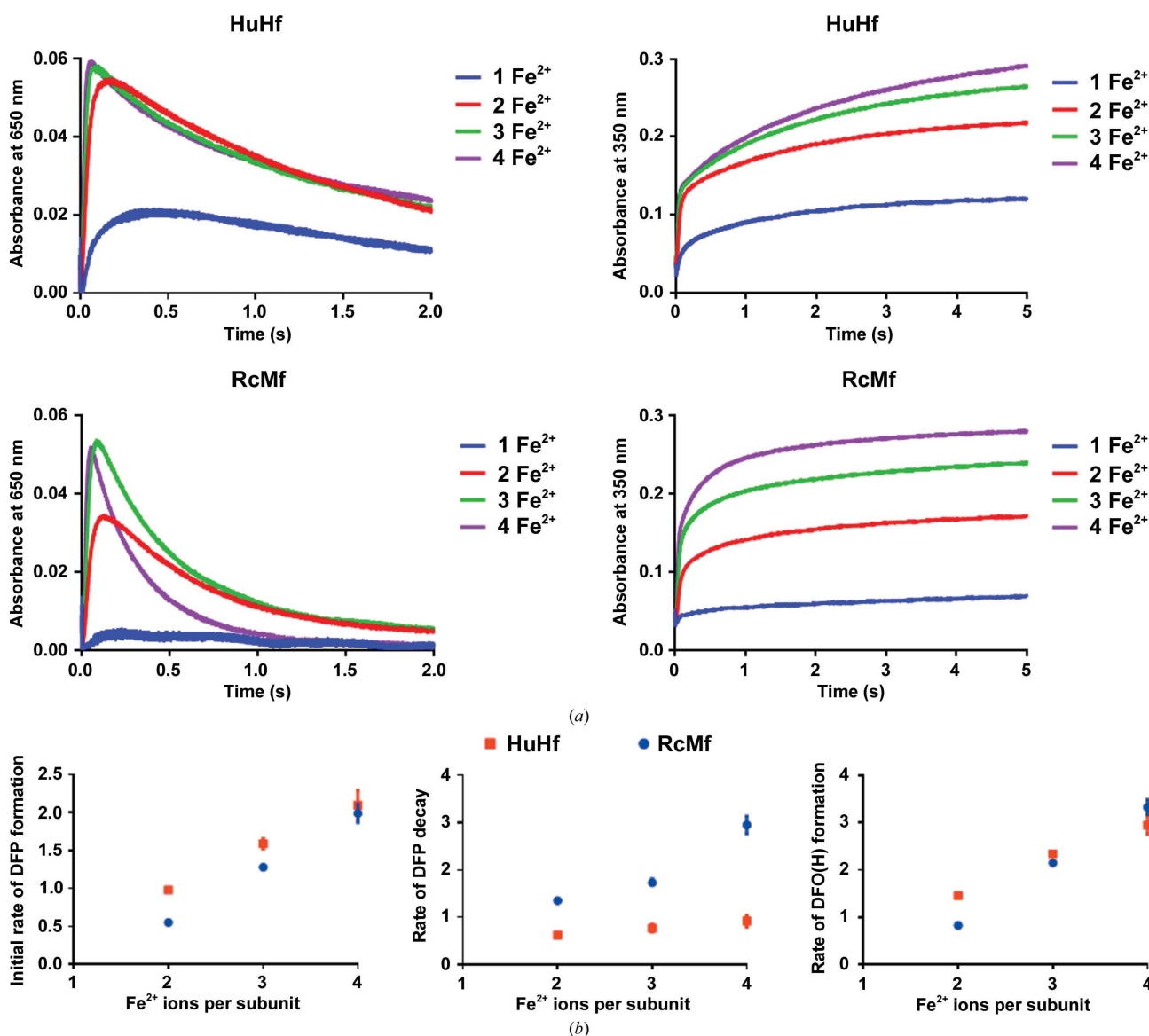


Figure 6
(a) The catalytic reaction rates in HuHf and RcMf are differently modulated by the $Fe^{2+}$:subunit ratio. Comparison of the reaction kinetics of the formation of (left) the intermediate DFP ($A_{650\ nm}$) and (right) the products DFO(H) ($A_{350\ nm}$) after the addition of one, two, three and four $Fe^{2+}$ ions per subunit to HuHf (upper panels) and RcMf (lower panels). (b) The panels show the dependency on the $Fe^{2+}$:subunit ratio of the initial rates of the formation of DFP (left), the decay of DFP (middle) and the formation of DFO(H) (right).
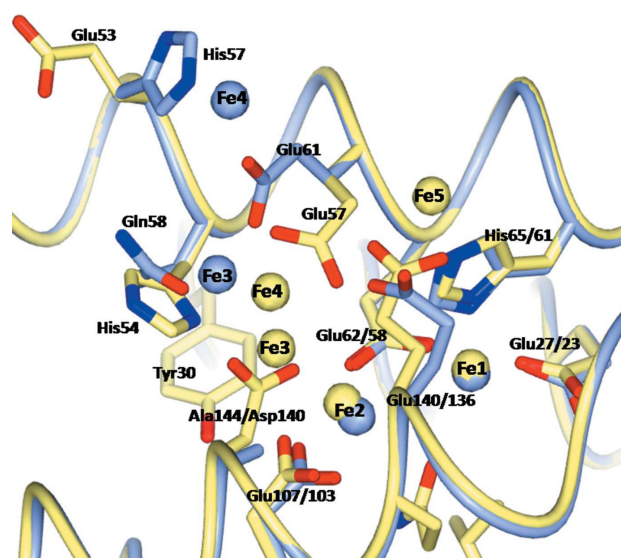
## HuHf



100 nm

## RcMf



100 nm
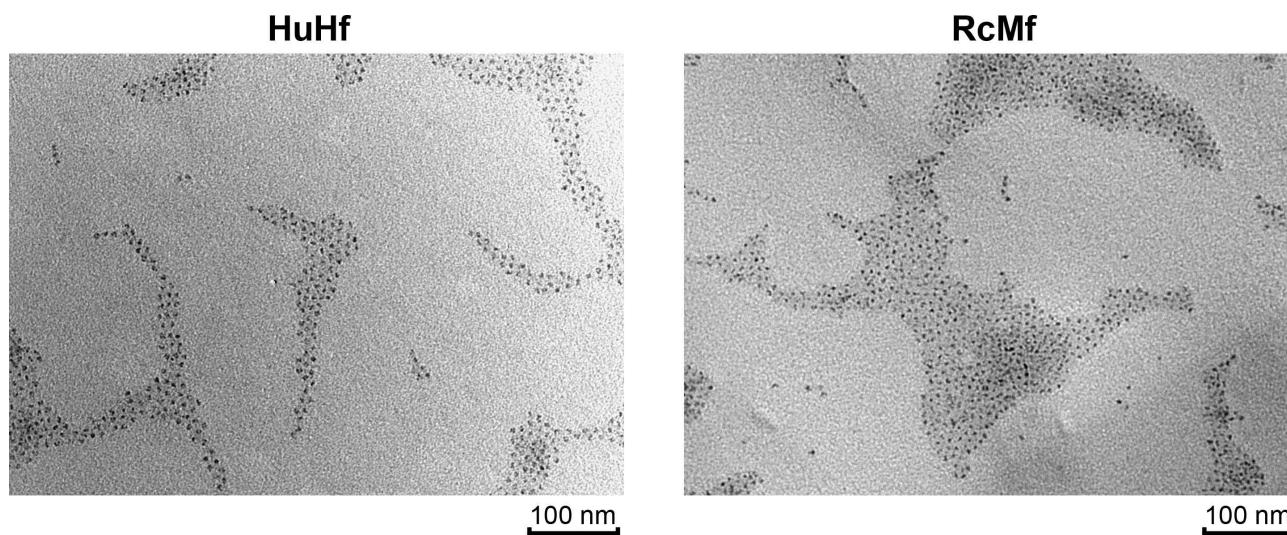
**Figure 7**
Biomineral core characterization. Representative TEM micrographs of HuHf and RcMf caged biominerals obtained from 2.5 $\mu M$ solutions of each protein mineralized with ferrous sulfate (80 $Fe^{2+}$ ions per subunit). The samples are not negatively stained; thus, the observed density represents the iron core within ferritin and not the protein.

A possible explanation of such differences can be found by analyzing the only experimental findings that can be correlated with the oxidation state of the iron ions in our structures, namely the coordination distances and the iron-coordination geometry.

The Fe1–Fe2 distance in all HuHf structures remains remarkably constant at a value of 3.49 Å, which is the same (within error) as that found in mixed-valence model compounds (3.53–3.62 Å)[1] (Majumdar *et al.*, 2014) and in the mixed-valence structure of methane monooxygenase, where an iron(II)–iron(III) distance of 3.4 Å has been reported (2.07 Å resolution; Whittington & Lippard, 2001). The Fe1–Fe2 distance observed in HuHf is the same as that observed in the crystal obtained under anaerobic conditions, but differs from the same distances found in RcMf structures at similar resolution, which appear to be longer and to vary between 3.5 and 3.8 Å, suggesting the presence of an iron(II)–iron(II) dinuclear cluster in this case. Despite the similarity of the Fe1–Fe2 distance in aerobic and anaerobic HuHf, their coordination numbers and geometries differ, but in the anaerobic crystal their geometry is the same as that found in RcMf. In summary, our data provide some support for the hypothesis that Fe1 and Fe2 form a mixed-valence dinuclear cluster in aerobic HuHf after 5 min of exposure to iron under aerobic conditions. In other words, the 1 min structure is most probably showing the binding of iron(II) ions, while the 5, 15 and 30 min structures may show the occurrence of a mixed-valence Fe1–Fe2 cluster. Clearly, the distinction of a mixed-valence from a fully reduced iron cluster cannot rest on crystallography alone, but comparison between the HuHf and RcMf structures obtained

under the same experimental conditions clearly shows differences in coordination geometry and intermetal distances, indicating a different chemical environment for the iron ions in the two proteins.

The measured differences in the dependence of the reaction rates on iron concentration between RcMf and HuHf most probably reflect the different amino-acid composition of the OS and the different chemical environment of the iron ions. Consequently, the slower rate of DFP decomposition in HuHf



**Figure 8**
Least-squares superimposition of the OS of HuHf (pale blue ribbon) and RcMf (pale yellow ribbon). The different locations and ligands of the Fe3, Fe4 and Fe5 iron-binding sites are evident. The amino acids are represented as sticks coloured following the colour of the parent protein backbone.

---

[1] See Cambridge Structural Database codes NIXLIR and NIXLUD for mixed-valence compounds in which the iron(II)–iron(III) distances are 3.53–3.62 Å; for comparison the iron(III)–iron(III) distances in ferric oxo(hydroxo) bridged compounds are 3.1 Å (codes NIXMAK and VARYOC10).

with respect to RcMf provides support for our hypothesis of having possibly trapped intermediate dioxygen species in our structures.

As can be appreciated from Fig. 8, the replacement of RcMf residues Glu53, His54 and Asp140 with His57, Gln58 and Ala144, respectively, results in the net loss of two negative charges and in different ligand strengths towards iron ions in the HuHf oxidoreductase site. Consequently, it is not surprising that the kinetic data show different profiles for the same iron loading of the two enzymes and markedly different decay rates of the DFP intermediate.

The differences between HuHf and RcMf do not end at the Fe1 and Fe2 sites. Fig. 8 shows the superposition of the 15 min structures of HuHf and RcMf, showing the different number and coordination of iron ions to the OS, which varies following the amino-acid variations of the two ferritins. For example, Fe3 in RcMf is bound only to His54, while in HuHf it is bound to Gln58 and Glu61 and occupies a different location. In RcMf Fe4 is bound to Glu57 (the analogous residue to Glu61 in HuHf) and to Asp140. In HuHf, Asp140 is substituted by the noncoordinating Ala144; hence, the fourth iron ion is bound to His57 in HuHf, which replaces Glu53 in RcMf. In the present structures, Glu61 is found bridging Fe3 and Fe4, supporting the hypothesis that it plays a role in driving iron ions to/from the ferroxidase site (Honarmand Ebrahimi *et al.*, 2012; Lawson *et al.*, 1991).

In summary, both the crystallographic and the stopped-flow data clearly show the existence of relevant structural and kinetic differences between RcMf and HuHf and confirm that beyond the Fe1 and Fe2 sites, which remain structurally constant, the additional iron-binding sites follow the chemical characteristics of the amino acids present in the OS and play a relevant role in the enzymatic reaction. Based on the reported evidence, the postulated third iron-binding site, which is a common characteristic of all ferritins (Honarmand Ebrahimi *et al.*, 2012, 2015), does not exist as a specific, well defined metal-coordination site, but is rather a region extending up to about 10 Å from the Fe1 and Fe2 sites where heterogeneous iron-anchoring points in ferritins of different origin are present.

## 5. Related literature

The following reference is cited in the Supporting Information for this article: Rice *et al.* (2000).

## References

Arosio, P., Ingrassia, R. & Cavadini, P. (2009). *Biochim. Biophys. Acta*, **1790**, 589–599.

Bernacchioni, C., Ciambellotti, S., Theil, E. C. & Turano, P. (2015). *Biochim. Biophys. Acta*, **1854**, 1118–1122.

Bernacchioni, C., Ghini, V., Pozzi, C., Di Pisa, F., Theil, E. C. & Turano, P. (2014). *Chem. Biol.* **9**, 2517–2525.

Bertini, I., Lalli, D., Mangani, S., Pozzi, C., Rosa, C., Theil, E. C. & Turano, P. (2012). *J. Am. Chem. Soc.* **134**, 6169–6176.

Bou-Abdallah, F., Arosio, P., Levi, S., Janus-Chandler, C. & Chasteen, N. D. (2003). *J. Biol. Inorg. Chem.* **8**, 489–497.

Bou-Abdallah, F., Arosio, P., Santambrogio, P., Yang, X., Janus-Chandler, C. & Chasteen, N. D. (2002). *Biochemistry*, **41**, 11184–11191.

Bou-Abdallah, F., Papaefthymiou, G. C., Scheswohl, D. M., Stanga, S. D., Arosio, P. & Chasteen, N. D. (2002). *Biochem J.* **364**, 57–63.

Bou-Abdallah, F., Yang, H., Awomolo, A., Cooper, B., Woodhall, M. R., Andrews, S. C. & Chasteen, N. D. (2014). *Biochemistry*, **53**, 483–495.

Bradley, J. M., Moore, G. R. & Le Brun, N. E. (2014). *J. Biol. Inorg. Chem.* **19**, 775–785.

Crichton, R. R. & Declercq, J.-P. (2010). *Biochim. Biophys. Acta*, **1800**, 706–718.

Ebrahimi, K. H., Hagedoorn, P. L., van der Weel, L., Verhaert, P. D. & Hagen, W. R. (2012). *J. Biol. Inorg. Chem.* **17**, 975–985.

Emsley, P., Lohkamp, B., Scott, W. G. & Cowtan, K. (2010). *Acta Cryst.* D**66**, 486–501.

Evans, P. (2006). *Acta Cryst.* D**62**, 72–82.

Evans, P. R. (2011). *Acta Cryst.* D**67**, 282–292.

Haldar, S., Bevers, L. E., Tosha, T. & Theil, E. C. (2011). *J. Biol. Chem.* **286**, 25620–25627.

Honarmand Ebrahimi, K., Bill, E., Hagedoorn, P. L. & Hagen, W. R. (2012). *Nature Chem. Biol.* **8**, 941–948.

Honarmand Ebrahimi, K., Hagedoorn, P. L. & Hagen, W. R. (2015). *Chem. Rev.* **115**, 295–326.

Hwang, J., Krebs, C., Huynh, B. H., Edmondson, D. E., Theil, E. C. & Penner-Hahn, J. E. (2000). *Science*, **287**, 122–125.

Karlsson, A., Parales, J. V., Parales, R. E., Gibson, D. T., Eklund, H. & Ramaswamy, S. (2003). *Science*, **299**, 1039–1042.

Langer, G., Cohen, S. X., Lamzin, V. S. & Perrakis, A. (2008). *Nature Protoc.* **3**, 1171–1179.

Laskowski, R. A., MacArthur, M. W., Moss, D. S. & Thornton, J. M. (1993). *J. Appl. Cryst.* **26**, 283–291.

Lawson, D. M., Artymiuk, P. J., Yewdall, S. J., Smith, J. M., Livingstone, J. C., Treffry, A., Luzzago, A., Levi, S., Arosio, P., Cesareni, G., Thomas, C. D., Shaw, W. V. & Harrison, P. M. (1991). *Nature (London)*, **349**, 541–544.

Leslie, A. G. W. (2006). *Acta Cryst.* D**62**, 48–57.

Liu, X. & Theil, E. C. (2005). *Acc. Chem. Res.* **38**, 167–175.

Majumdar, A., Apfel, U.-P., Jiang, Y., Moënne-Loccoz, P. & Lippard, S. J. (2014). *Inorg. Chem.* **53**, 167–181.

Marchetti, A., Parker, M. S., Moccia, L. P., Lin, E. O., Arrieta, A. L., Ribalet, F., Murphy, M. E. P., Maldonado, M. T. & Armbrust, E. V. (2009). *Nature (London)*, **457**, 467–470.

Masuda, T., Goto, F., Yoshihara, T. & Mikami, B. (2010). *Biochem. Biophys. Res. Commun.* **400**, 94–99.

McNicholas, S., Potterton, E., Wilson, K. S. & Noble, M. E. M. (2011). *Acta Cryst.* D**67**, 386–394.

Mirica, L. M., Ottenwaelder, X. & Stack, T. D. (2004). *Chem. Rev.* **104**, 1013–1046.

Mirica, L. M., Rudd, D. J., Vance, M. A., Solomon, E. I., Hodgson, K. O., Hedman, B. & Stack, T. D. (2006). *J. Am. Chem. Soc.* **128**, 2654–2665.

Murshudov, G. N., Skubák, P., Lebedev, A. A., Pannu, N. S., Steiner, R. A., Nicholls, R. A., Winn, M. D., Long, F. & Vagin, A. A. (2011). *Acta Cryst.* D**67**, 355–367.

Nagano, S. & Poulos, T. L. (2005). *J. Biol. Chem.* **280**, 31659–31663.

Pfaffen, S., Abdulqadir, R., Le Brun, N. E. & Murphy, M. E. P. (2013). *J. Biol. Chem.* **288**, 14917–14925.

Pozzi, C., Di Pisa, F., Lalli, D., Rosa, C., Theil, E., Turano, P. & Mangani, S. (2015). *Acta Cryst.* D**71**, 941–953.

Rice, P., Longden, I. & Bleasby, A. (2000). *Trends Genet.* **16**, 276–277.

Schlichting, I., Berendzen, J., Chu, K., Stock, A. M., Maves, S. A., Benson, D. E., Sweet, R. M., Ringe, D., Petsko, G. A. & Sligar, S. G. (2000). *Science*, **287**, 1615–1622.

Stillman, T. J., Hempstead, P. D., Artymiuk, P. J., Andrews, S. C., Hudson, A. J., Treffry, A., Guest, J. R. & Harrison, P. M. (2001). *J. Mol. Biol.* **307**, 587–603.

Tatur, J., Hagen, W. R. & Matias, P. M. (2007). *J. Biol. Inorg. Chem.* **12**, 615–630.

Theil, E. C. (2011). *Curr. Opin. Chem. Biol.* **15**, 304–311.

Theil, E. C., Behera, R. K. & Tosha, T. (2013). *Coord. Chem. Rev.* **257**, 579–586.

Theil, E. C., Turano, P., Ghini, V., Allegrozzi, M. & Bernacchioni, C. (2014). *J. Biol. Inorg. Chem.* **19**, 615–622.

Tosha, T., Behera, R. K. & Theil, E. C. (2012). *Inorg. Chem.* **51**, 11406–11411.

Treffry, A., Zhao, Z., Quail, M. A., Guest, J. R. & Harrison, P. M. (1997). *Biochemistry*, **36**, 432–441.

Vagin, A. & Teplyakov, A. (2010). *Acta Cryst.* D**66**, 22–25.

Whittington, D. A. & Lippard, S. J. (2001). *J. Am. Chem. Soc.* **123**, 827–838.

Winn, M. D. *et al.* (2011). *Acta Cryst.* D**67**, 235–242.

# ORDER FORM

> YOU WILL AUTOMATICALLY BE SENT DETAILS OF HOW TO DOWNLOAD
> AN ELECTRONIC REPRINT OF YOUR PAPER, FREE OF CHARGE.
> PRINTED REPRINTS MAY BE PURCHASED USING THIS FORM.

Please scan your order and send to lj@iucr.org

**INTERNATIONAL UNION OF CRYSTALLOGRAPHY**
5 Abbey Square
Chester CH1 2HU, England.

VAT No. GB 161 9034 76

Article No.: D151307-DW5141

Title of article     Iron binding to human heavy-chain ferritin

Name  Stefano Mangani

Address  CERM, University of Florence, Via Della Lastruccia 3, Sesto Fiorentino, 50019 Firenze, Italy

E-mail address (for electronic reprints)     stefano.mangani@unisi.it

## OPEN ACCESS

IUCr journals offer authors the chance to make their articles open access on **Crystallography Journals Online**. For full details of our open-access policy, see http://journals.iucr.org/services/openaccess.html. For authors in European Union countries, VAT will be added to the open-access charge.

☐ I wish to make my article open access. The charge for making an article open access is **1200 United States dollars**.

## DIGITAL PRINTED REPRINTS

I wish to order  . . . . . . .  paid reprints

**These reprints will be sent to the address given above. If the above address or e-mail address is not correct, please indicate an alternative:**

## PAYMENT

Charge for open access     **1200**     USD     Charge for reprints . . . . . . . . USD     Total charge  . . . . . . . USD

☐ A cheque for  . . . . . . .  USD payable to **INTERNATIONAL UNION OF CRYSTALLOGRAPHY** is enclosed

☐ I have an open-access voucher to the value of  . . . . . . . USD

Voucher No.

☐ An official purchase order made out to **INTERNATIONAL UNION OF CRYSTALLOGRAPHY**  ☐ is enclosed  ☐ will follow

Purchase order No.

☐ Please invoice me

☐ I wish to pay by credit card

Date

Signature

## OPEN ACCESS

The charge for making an article open access is **1200 United States dollars**. For authors in European Union countries, VAT will be added to the open-access charge.

A paper may be made open access at any time after the proof stage on receipt of the appropriate payment. This includes all back articles on **Crystallography Journals Online**. For further details, please contact support@iucr.org. Likewise, organizations wishing to sponsor open-access publication of a series of articles or complete journal issues should contact support@iucr.org.

## DIGITAL PRINTED REPRINTS

An electronic reprint is supplied free of charge.

Printed reprints without limit of number may be purchased at the prices given in the table below. The requirements of all joint authors, if any, and of their laboratories should be included in a single order, specifically ordered on the form overleaf. All orders for reprints must be submitted promptly.

Prices for reprints are given below in **United States dollars** and include postage.

| Number of reprints required | Size of paper (in printed pages) | | | | |
|---|---|---|---|---|---|
| | 1–2 | 3–4 | 5–8 | 9–16 | Additional 8's |
| 50 | 184 | 268 | 372 | 560 | 246 |
| 100 | 278 | 402 | 556 | 842 | 370 |
| 150 | 368 | 534 | 740 | 1122 | 490 |
| 200 | 456 | 664 | 920 | 1400 | 610 |
| Additional 50's | 86 | 128 | 178 | 276 | 116 |

## PAYMENT AND ORDERING

Cheques should be in **United States dollars** payable to **INTERNATIONAL UNION OF CRYSTALLOGRAPHY**. Official purchase orders should be made out to **INTERNATIONAL UNION OF CRYSTALLOGRAPHY**.

Orders should be returned by email to lj@iucr.org

## ENQUIRIES

Enquiries concerning reprints should be sent to support@iucr.org.